

## Polygonal finite elements for incompressible fluid flow

Cameron Talischi<sup>1</sup>, Anderson Pereira<sup>2</sup>, Glaucio H. Paulino<sup>1,\*</sup>, Ivan F. M. Menezes<sup>2</sup>  
and Márcio S. Carvalho<sup>2</sup>

<sup>1</sup>*University of Illinois at Urbana-Champaign, USA*

<sup>2</sup>*Pontifical Catholic University of Rio de Janeiro (PUC-Rio), Brazil*

### SUMMARY

We discuss the use of polygonal finite elements for analysis of incompressible flow problems. It is well-known that the stability of mixed finite element discretizations is governed by the so-called inf-sup condition, which, in this case, depends on the choice of the discrete velocity and pressure spaces. We present a low-order choice of these spaces defined over convex polygonal partitions of the domain that satisfies the inf-sup condition and, as such, does not admit spurious pressure modes or exhibit locking. Within each element, the pressure field is constant while the velocity is represented by the usual isoparametric transformation of a linearly-complete basis. Thus, from a practical point of view, the implementation of the method is classical and does not require any special treatment. We present numerical results for both incompressible Stokes and stationary Navier–Stokes problems to verify the theoretical results regarding stability and convergence of the method. Copyright © 2013 John Wiley & Sons, Ltd.

Received 22 January 2013; Revised 16 July 2013; Accepted 1 August 2013

KEY WORDS: polygonal finite elements; mixed variational problems; incompressible flow; Stokes and Navier–Stokes equations; Voronoi meshes

### 1. INTRODUCTION

The literature on finite element methods for analysis of incompressible flow is vast and growing (we refer to the monographs on the topic [1–5] for a more exhaustive survey of the existing methods). Stability is a critical issue concerning mixed finite element formulations, and it is well-known that it is dictated by the so-called inf-sup condition [6, 7]. Roughly speaking, in the present context, the inf-sup condition delineates the appropriate balance between the velocity and pressure approximations. The velocity space must be sufficiently rich in order to appropriately approximate the flow characteristics in spite of the weak incompressibility constraint whose degree of enforcement is determined by the choice of pressure space. Selecting too large a pressure space can overconstrain the velocity field in turn leading to poor convergence (or non-convergence) and possibly a rank-deficiency in the system in the form of pressure modes.

It turns out that many natural choices for the velocity–pressure approximation are not stable. For example, in the case of element-wise constant pressure approximations (the lowest possible order), piecewise linear velocities on simplicial meshes in general exhibit locking while piecewise bilinear (trilinear, resp.) velocities on quadrilateral (hexahedral, resp.) meshes can lead to spurious checkerboard modes. Equal-order discretizations are similarly unstable.

As low-order schemes are attractive from a computational perspective in many practical engineering applications, there are several approaches satisfying the inf-sup condition for such schemes.

---

\*Correspondence to: Glaucio H. Paulino, University of Illinois at Urbana-Champaign, USA.

†E-mail: paulino@uiuc.edu

For example, one approach is to introduce enrichments to the velocity space in the form of internal or edge bubble functions. A well-known example is the MINI element of Arnold *et al.* [8]. Stabilization methods that introduce residual or penalty terms to augment the variational statement of the problem have also been successfully applied to obtain stable low-order formulations <sup>‡</sup> (see, for example, [9–11]). However, mesh-dependent parameters in such formulations must be chosen carefully, and special data structures may be needed for the numerical implementation [12]. In this regard, we mention the recent work [13], based on local projection operators, which addresses the aforementioned shortcomings. Finally, certain mesh topologies have been shown to be stable even when the underlying spaces are in general not inf-sup compatible. One example is the macroelement mesh in [14], which consists of a special arrangement of quadrilaterals. Another related approach is due to Hauret *et al.* [15] where ‘diamond’ meshes are constructed from simplicial partitions of the domain and the choice of spaces together with the special structure of the mesh ensure stability.

As illustrated in this paper, *low-order velocity and pressure approximations based on a large class of polygonal discretizations satisfy the inf-sup condition without the need for any additional treatment.* Intuitively, this stability can be attributed to the presence of more velocity DOFs for polygonal elements with many sides (per pressure DOF) when compared to triangular and quadrilateral discretizations. We remark that we have observed similar characteristics of polygonal discretizations in topology optimization [16–19] where spurious checkerboard-like patterns also plague triangular and quadrilateral discretizations [20].

While the development of polygonal finite elements has had a long history, dating back to the seminal work of Wachspress [21], their numerical implementation and application to solving PDEs is more recent (see, for example, [22–25]). From a practical perspective, the greater flexibility for mesh generation is an attractive feature of polygonal finite elements. On the one hand, local modifications of the mesh (e.g., refinement through element splitting used in [26]) is made possible by the fact that not all the elements have to be topologically equivalent. On the other hand, a number of mesh generation algorithms, harnessing the properties of Voronoi diagrams, have been developed recently [27–30]. In addition to advantages in mesh generation, polygonal finite elements can outperform their triangular and quadrilateral counterparts in terms of accuracy (see the example in section 3.2 of [17] where the overall system size can be smaller for a given level of error).

Recently, a number of mimetic finite difference (MFD) schemes have been developed for solving PDEs on polygonal and polyhedral meshes. While some MFD formulations (e.g., [31]) are closely related to mixed finite elements, purely nodal MFD schemes (e.g., [32, 33]) are related to primal finite elements. This connection is elucidated in the recent work [34] wherein an FEM-like incarnation of MFD, labeled Virtual Element Method, is developed. Of particular relevance to the present work are the MFD formulations for incompressible Stokes flow for polygonal meshes reported in [35, 36]. While the formulation in [35] features edge DOFs for the velocity field, the results in [36] delineate the conditions on the mesh topology under which nodal velocity DOFs are sufficient to ensure stability. For meshes consisting of convex elements, one such scenario is when each interior node is incident to at most three edges. This property naturally excludes triangular and quadrilateral grids and requires the elements to have many sides. Even though in the mimetic framework an explicit construction of the basis functions is not needed, the present finite element scheme is a realization of the MFD formulation considered in [36]. Thus, as we will show later in Section 5, the results of [36] are applicable to our formulation.

The remainder of this paper is organized as follows: in the next section, we introduce the problem of incompressible Stokes flow, which serves as the model problem for the theoretical discussion. In Section 3, we present the mixed variational finite element discretization of the problem and discuss sufficient conditions for convergence. Next, in Section 4, we show the construction of the low-order velocity and pressure space for convex polygonal meshes. The specific condition on the mesh topology that is sufficient for stability is discussed and verified in Section 5. Numerical results demonstrating convergence of the method for both Stokes and stationary Navier–Stokes problems are provided in Section 6. We conclude the paper with some remarks in Section 7.

<sup>‡</sup>In some instances, one can establish an equivalence between enrichment and stabilized methods (see, for example [37]).

We briefly and partially introduce the notation adopted in this paper. We denote by  $H^k(\Omega)$  the standard Sobolev space consisting of functions whose derivatives up to the  $k$ th order are square-integrable over the given domain  $\Omega$  and write  $\|\cdot\|_k$  for its norm. We write  $L^2(\Omega) = H^0(\Omega)$  and denote by  $H_0^1(\Omega)$  functions in  $H^1(\Omega)$  that vanish on the boundary  $\partial\Omega$ . For any subset  $E \subseteq \Omega$ , we denote by  $|E|$  its measure and by  $\chi_E$  its characteristic (or indicator) function. This means that  $\chi_E(\mathbf{x}) = 1$  if  $\mathbf{x} \in E$  and  $\chi_E(\mathbf{x}) = 0$  if  $\mathbf{x} \in \Omega \setminus E$ . The interior of  $E$  is denoted by  $\text{int}(E)$  and its closure by  $\overline{E}$ .

## 2. MODEL PROBLEM: INCOMPRESSIBLE STOKES FLOW

Let  $\Omega$  denote an open bounded domain in  $\mathbb{R}^2$  with polygonal boundary. The incompressible Stokes flow problem is given by

$$\begin{aligned} -2 \operatorname{div} [\nu \boldsymbol{\epsilon}(\mathbf{u})] + \nabla p &= \mathbf{f} & \text{in } \Omega \\ \operatorname{div} \mathbf{u} &= \mathbf{0} & \text{in } \Omega \\ \mathbf{u} &= \mathbf{0} & \text{on } \partial\Omega \end{aligned} \quad (1)$$

where  $\mathbf{u}$  and  $p$  are the velocity and modified pressure (pressure divided by density) fields, respectively,  $\boldsymbol{\epsilon}(\mathbf{u}) = (\nabla \mathbf{u} + \nabla^T \mathbf{u})/2$  is the rate-of-strain tensor,  $\mathbf{f} \in [L^2(\Omega)]^2$  is the applied body force per unit of mass and  $\nu > 0$  is the kinematic viscosity of the fluid. Defining the velocity and pressure spaces

$$\mathcal{V} = [H_0^1(\Omega)]^2 \quad \text{and} \quad \mathcal{Q} = L_0^2(\Omega) := \{q \in L^2(\Omega) : \int_{\Omega} q \, dx = 0\} \quad (2)$$

the mixed variational form of (1) consists of finding  $(\mathbf{u}, p) \in \mathcal{V} \times \mathcal{Q}$  such that

$$a(\mathbf{u}, \mathbf{v}) + b(p, \mathbf{v}) = \ell(\mathbf{v}), \quad \forall \mathbf{v} \in \mathcal{V} \quad (3)$$

$$b(q, \mathbf{u}) = 0, \quad \forall q \in \mathcal{Q} \quad (4)$$

where

$$a(\mathbf{u}, \mathbf{v}) = 2 \int_{\Omega} \nu \boldsymbol{\epsilon}(\mathbf{u}) : \boldsymbol{\epsilon}(\mathbf{v}) \, dx, \quad b(p, \mathbf{v}) = - \int_{\Omega} p \operatorname{div} \mathbf{v} \, dx, \quad \ell(\mathbf{v}) = \int_{\Omega} \mathbf{f} \cdot \mathbf{v} \, dx \quad (5)$$

A sufficient set of conditions for the well-posedness of the abstract variational problem (3)–(4) is that bilinear forms  $a(\cdot, \cdot)$  and  $b(\cdot, \cdot)$  and the linear form  $\ell(\cdot)$  are continuous,  $a(\cdot, \cdot)$  is coercive on  $\mathcal{V}^0 := \{\mathbf{v} \in \mathcal{V} : b(q, \mathbf{v}) = 0, \forall q \in \mathcal{Q}\}$ , that is,

$$\exists \alpha > 0 \quad \text{such that} \quad a(\mathbf{v}, \mathbf{v}) \geq \alpha \|\mathbf{v}\|_{\mathcal{V}}^2, \quad \forall \mathbf{v} \in \mathcal{V}^0 \quad (6)$$

and there exists a constant  $\beta > 0$  such that

$$\inf_{q \in \mathcal{Q} \setminus \{0\}} \sup_{\mathbf{v} \in \mathcal{V} \setminus \{0\}} \frac{b(q, \mathbf{v})}{\|q\|_{\mathcal{Q}} \|\mathbf{v}\|_{\mathcal{V}}} \geq \beta \quad (7)$$

The last condition is the continuous inf-sup condition.

In the Stokes problem, the natural norms associated with the velocity and pressure spaces are

$$\|\mathbf{v}\|_{\mathcal{V}} := \|\nabla \mathbf{v}\|_0, \quad \|q\|_{\mathcal{Q}} := \|q\|_0 \quad (8)$$

and one can show, using Korn's inequalities [38], that  $a(\cdot, \cdot)$  is continuous and coercive on  $\mathcal{V}$  (and subsequently on  $\mathcal{V}^0$ ). Continuity of  $b(\cdot, \cdot)$  and  $\ell(\cdot)$  is also straightforward to verify. Finally, the condition (7) follows from the fact that the divergence operator is a surjection from  $[H_0^1(\Omega)]^2$  onto  $L_0^2(\Omega)$  [1].

For the sake of simplicity, we have assumed that only homogenous velocity boundary conditions are imposed in the model problem (1). However, the same abstract variational problem can be obtained for inhomogenous boundary conditions by 'lifting' the boundary conditions and changing variables [4]. The theoretical results also hold when the velocity boundary conditions are imposed on  $\Gamma_D \subsetneq \partial\Omega$ ,  $|\Gamma_D| \neq 0$  because  $\|\nabla \mathbf{v}\|_0$  will again define a norm for the velocity space  $\{\mathbf{v} \in [H^1(\Omega)]^2 : \mathbf{v} = \mathbf{0} \text{ on } \Gamma_D\}$ .

3. FINITE ELEMENT APPROXIMATION

Considering the finite element subspaces  $\mathcal{V}_h \subseteq \mathcal{V}$  and  $\mathcal{Q}_h \subseteq \mathcal{Q}$ , with  $h$  indicating the maximum diameter of elements in the underlying mesh, the Galerkin approximation of (3)–(4) consists of seeking  $(\mathbf{u}_h, p_h) \in \mathcal{V}_h \times \mathcal{Q}_h$  such that

$$a(\mathbf{u}_h, \mathbf{v}_h) + b(p_h, \mathbf{v}_h) = \ell(\mathbf{v}_h), \quad \forall \mathbf{v}_h \in \mathcal{V}_h \tag{9}$$

$$b(q_h, \mathbf{u}_h) = 0, \quad \forall q_h \in \mathcal{Q}_h \tag{10}$$

The approximate problem (9)–(10) is well-posed if, in addition to the previously stated continuity and coercivity requirements,

$$\beta_h := \inf_{q_h \in \mathcal{Q}_h \setminus \{0\}} \sup_{\mathbf{v}_h \in \mathcal{V}_h \setminus \{0\}} \frac{b(q_h, \mathbf{v}_h)}{\|q_h\|_{\mathcal{Q}} \|\mathbf{v}_h\|_{\mathcal{V}}} > 0 \tag{11}$$

This is nothing but the discrete version of the inf-sup condition (7) and is sometimes referred to as the Ladyzenskaja-Babuska-Brezzi or LBB condition [6, 7]. Observe that for the Stokes problem,  $a(\cdot, \cdot)$  is coercive on all of  $\mathcal{V}$ , and so it follows that it is also coercive on the subspace  $\mathcal{V}_h^0 := \{\mathbf{v}_h \in \mathcal{V}_h : b(q_h, \mathbf{v}_h) = 0, \forall q_h \in \mathcal{Q}_h\}$  §.

Moreover, under these conditions, the finite element solution pair  $(\mathbf{u}_h, p_h)$  satisfies the following error estimates [4]:

$$\|\mathbf{u} - \mathbf{u}_h\|_{\mathcal{V}} \leq \left(1 + \frac{c_a}{\alpha}\right) \left(1 + \frac{c_b}{\beta_h}\right) \inf_{\mathbf{v}_h \in \mathcal{V}_h} \|\mathbf{u} - \mathbf{v}_h\|_{\mathcal{V}} + \frac{c_b}{\alpha} \inf_{q_h \in \mathcal{Q}_h} \|p - q_h\|_{\mathcal{Q}} \tag{12}$$

$$\begin{aligned} \|p - p_h\|_{\mathcal{Q}} &\leq \frac{c_a}{\beta_h} \left(1 + \frac{c_a}{\alpha}\right) \left(1 + \frac{c_b}{\beta_h}\right) \inf_{\mathbf{v}_h \in \mathcal{V}_h} \|\mathbf{u} - \mathbf{v}_h\|_{\mathcal{V}} \\ &\quad + \left(1 + \frac{c_b}{\beta_h} + \frac{c_a c_b}{\alpha \beta_h}\right) \inf_{q_h \in \mathcal{Q}_h} \|p - q_h\|_{\mathcal{Q}} \end{aligned} \tag{13}$$

for some positive constants  $c_a$  and  $c_b$  ¶.

With the typical choice of finite element spaces, standard interpolation error estimates show that the distances  $\inf_{\mathbf{v}_h \in \mathcal{V}_h} \|\mathbf{v} - \mathbf{v}_h\|_{\mathcal{V}}$  and  $\inf_{q_h \in \mathcal{Q}_h} \|p - q_h\|_{\mathcal{Q}}$  vanish under mesh refinement as  $h \rightarrow 0$ . The estimates (12)–(13) then prove convergence of the finite element solutions *provided that  $\beta_h$  remains bounded away from zero*. More specifically, if  $\beta_h \geq \beta_0$  for some fixed constant  $\beta_0 > 0$  and all  $h$ , then the distance between  $(\mathbf{u}, p)$  and  $(\mathbf{u}_h, p_h)$  is on the order of the distance between  $(\mathbf{u}, p)$  and its best approximation in  $\mathcal{V}_h \times \mathcal{Q}_h$ , and the method achieves an optimal rate of convergence. Otherwise, if  $\beta_h \rightarrow 0$  with  $h$ , the finite element formulation is said to exhibit *locking*. Intuitively, locking occurs when, given a finite element pressure space  $\mathcal{Q}_h$ , the velocity space  $\mathcal{V}_h$  is not sufficiently rich to both satisfy the weak incompressibility constraint (4) and approximate the flow characteristics. Mesh refinement does not alleviate the problem because it also enriches the pressure space  $\mathcal{Q}_h$ . Therefore, it is important to recognize that preventing locking involves the appropriate selection of  $\mathcal{V}_h$  with respect to the given choice of pressure discretization.

Aside from locking, the other important issue related to stability of the mixed finite element formulations is the appearance of spurious modes. The pair of spaces  $\mathcal{V}_h$  and  $\mathcal{Q}_h$  admits a *spurious pressure mode* if there exists  $\tilde{p}_h \in \mathcal{Q}_h \setminus \{0\}$  such that

$$b(\tilde{p}_h, \mathbf{v}_h) = 0 \quad \forall \mathbf{v}_h \in \mathcal{V}_h \tag{14}$$

§In general, coercivity of  $a(\cdot, \cdot)$  on  $\mathcal{V}^0$  does not imply its coercivity on  $\mathcal{V}_h^0$  because we may have  $\mathcal{V}_h^0 \not\subseteq \mathcal{V}^0$ . In such cases, the latter must be verified independently for the given spaces  $\mathcal{V}_h$  and  $\mathcal{Q}_h$ .

¶These constants are in fact the norms associated with the bilinear forms  $a(\cdot, \cdot)$  and  $b(\cdot, \cdot)$ . Notice that in these estimates, we have used the fact that  $a(\cdot, \cdot)$  is  $\alpha$ -coercive on  $\mathcal{V}_h^0$  (see the remark in the previous footnote).

If pressure modes are present, then the discrete inf-sup condition (11) cannot be satisfied (the stability constant  $\beta_h$  is simply zero), and so the finite element problem is not well-posed. Observe that if  $(\mathbf{u}_h, p_h)$  is the solution to (9)–(10), then  $(\mathbf{u}_h, p_h + s\tilde{p}_h)$  is also a solution for any  $s \in \mathbb{R}$  and a spurious pressure mode  $\tilde{p}_h$ . Conversely, for finite-dimensional spaces  $\mathcal{V}_h$  and  $\mathcal{Q}_h$ , the violation of the discrete inf-sup condition implies existence of spurious modes. We note that the appearance of pressure modes is problem-dependent (for the same velocity–pressure pair, the pressure mode may or may not exist depending on the boundary conditions of the problem) while locking is more intrinsic to the degree of interpolation of velocity and pressure fields.

We conclude this brief discussion by noting that there exists certain improved error estimates, most notably for the bilinear-velocity constant-pressure element, which show that the approximate velocity solution in some cases can be accurate, despite the failure to satisfy the inf-sup condition [2, 39–42]. However, such elements can be unreliable in general and should be used only by knowledgeable practitioners. For example, the presence of spurious modes can lead to an ill-posed discrete problem (one with no solutions) when certain inhomogenous boundary conditions are prescribed (see, for example, [43, 44]).

#### 4. VELOCITY AND PRESSURE SPACES ON POLYGONAL DISCRETIZATIONS

In this section, we define a low-order pair of velocity and pressure spaces defined on polygonal meshes that leads to a stable finite element approximation. Consider a mesh  $\mathcal{T}_h = \{\Omega_m\}_{m=1}^M$  consisting of closed strictly convex polygons that form a partition of the domain  $\Omega$ <sup>‡</sup>. The mesh size  $h$  is the maximum diameter of the elements in  $\mathcal{T}_h$ . Aside from the usual shape-regularity assumptions, we must require certain conditions of the topology of  $\mathcal{T}_h$  in order to ensure the satisfaction of the inf-sup condition. These will be discussed in the next section.

We define the discrete pressure space  $\mathcal{Q}_h$  to simply consist of element-wise constant functions on  $\mathcal{T}_h$ , that is

$$\mathcal{Q}_h = \{q_h \in L^2_0(\Omega) : q_h|_{\Omega_m} = \text{constant}, \forall m = 1, \dots, M\} \quad (15)$$

This is, in some sense, the lowest possible order discretization for the pressure field. Observe that each admissible pressure function  $q_h \in \mathcal{Q}_h$  has the form

$$q_h = \sum_{m=1}^M c_m \chi_{\Omega_m} \quad (16)$$

where  $c_m$  is the constant value of  $q_h$  over the  $m$ th element (recall that  $\chi_{\Omega_m} \equiv 1$  on  $\Omega_m$  and vanishes elsewhere). However, because  $\int_{\Omega} q_h \, dx = 0$ , the coefficients must satisfy the following relation:

$$\sum_{m=1}^M c_m |\Omega_m| = 0 \quad (17)$$

In order to enforce the zero-mean condition, we consider the following set of pressure basis functions

$$\psi_m := \chi_{\Omega_m} - \frac{|\Omega_m|}{|\Omega_M|} \chi_{\Omega_M}, \quad m = 1, \dots, M-1 \quad (18)$$

Observe that  $\mathcal{Q}_h = \text{span}\{\psi_1, \dots, \psi_{M-1}\}$  and that the  $m$ th DOF, for  $1 \leq m \leq M-1$ , corresponds to the pressure in  $\Omega_m$  (we refer the reader to [45] for a more general discussion of such construction). Using the standard finite element approximation theory, we can show that for  $p \in H^\lambda(\Omega) \cap \mathcal{Q}$ , with  $0 < \lambda \leq 1$ , we have  $\inf_{q_h \in \mathcal{Q}_h} \|p - q_h\|_{\mathcal{Q}} = \mathcal{O}(h^\lambda)$ .

<sup>‡</sup>Therefore,  $\bigcup_{m=1}^M \Omega_m = \overline{\Omega}$  and  $\text{int}(\Omega_m) \cap \text{int}(\Omega_{m'}) = \emptyset$  if  $m \neq m'$ . By strictly convex, we mean that no three vertices of the polygon are collinear.

For the velocity space  $\mathcal{V}_h$ , we consider a conforming space where, as usual, the DOFs are associated with the interior vertices in the mesh. If  $N$  denotes the number of internal vertices of the mesh, then the velocity space has dimension  $2N$ . Over each polygonal element, the velocity field is represented by the expansion of an appropriate set of barycentric basis functions. By definition, the barycentric functions are non-negative and linearly complete (i.e., capable of representing any linear field exactly) and, as a result, satisfy the Lagrangian (Kronecker-delta) property and vary linearly on the boundary of the element [46]. The latter property, together with the choice of DOFs, ensures a conforming approximation.

Denoting by  $\mathcal{P}(E)$  the span of such basis over polygon  $E$ , the velocity space is defined as

$$\mathcal{V}_h = \left\{ \mathbf{v}_h \in [C^0(\bar{\Omega})]^2 \cap \mathcal{V} : \mathbf{v}_h|_{\Omega_m} \in [\mathcal{P}(\Omega_m)]^2 \quad \forall m = 1, \dots, M \right\} \tag{19}$$

A number of barycentric basis functions are available for general convex polygons, and we refer the reader to [23] for a review on the topic. We next proceed to describe the choice of  $\mathcal{P}(E)$  used in this work, which follows the isoparametric construction of [22]. The main advantage of using the isoparametric basis functions is that the element-level calculations are carried out over a reference (parent) domain, and as a result, the basis functions and the quadrature rule need to be computed, tabulated and stored once for each type of  $n$ -gon. This lowers the cost associated with the geometric construction of basis functions to a level comparable to that of traditional Lagrangian elements for which the basis functions have analytical expressions. Moreover, for triangles and quadrilaterals, the resulting finite elements coincide with the commonly used linear and isoparametric bilinear elements, respectively.

Consider a regular closed  $n$ -gon  $\hat{E}_n$  with vertices located at  $\xi_i = [\cos(2\pi i/n), \sin(2\pi i/n)]$  for  $i = 1, \dots, n$ . For  $\xi \in \text{int}(\hat{E}_n)$ , the *Wachspress* interpolation function corresponding to  $i$ th vertex is defined as [21, 46]

$$\hat{\varphi}_i(\xi) = \frac{w_i(\xi)}{\sum_{j=1}^n w_j(\xi)} \tag{20}$$

where  $w_i$  are given by \*\*

$$w_i(\xi) = \frac{A(\xi_{i-1}, \xi_i, \xi_{i+1})}{A(\xi_{i-1}, \xi_i, \xi)A(\xi_i, \xi_{i+1}, \xi)} \tag{21}$$

Here,  $A$  denotes the area of the triangle with vertices located at its arguments (Figure 1(a)). Because the  $n$ -gon is regular,  $A(\xi_{i-1}, \xi_i, \xi_{i+1})$  is the same for all  $i$  and thus can be factored out of expression (20). In particular, instead of (21), we can use

$$w_i(\xi) = \frac{1}{A(\xi_{i-1}, \xi_i, \xi)A(\xi_i, \xi_{i+1}, \xi)} \tag{22}$$

in (20).

It is immediate from the construction of  $\hat{\varphi}_i$  that they are positive in the interior of the polygon and form a partition of unity, that is, for  $\xi \in \text{int}(\hat{E}_n)$ ,

$$\sum_{i=1}^n \hat{\varphi}_i(\xi) = 1 \tag{23}$$

Moreover, one can show that (see, for example, the appendix of [47]),

$$\sum_{i=1}^n \hat{\varphi}_i(\xi)\xi_i = \xi \tag{24}$$

Observe that (23) and (24) indicate that any linear field can be represented by  $\hat{\varphi}_i$ , and so the *Wachspress* functions form a set of *barycentric* coordinates for the polygon  $\hat{E}_n$ . While  $\xi$  thus far

\*\*By convention, we set  $\xi_{n+1} = \xi_1$  and  $\xi_0 = \xi_n$  in this expression.

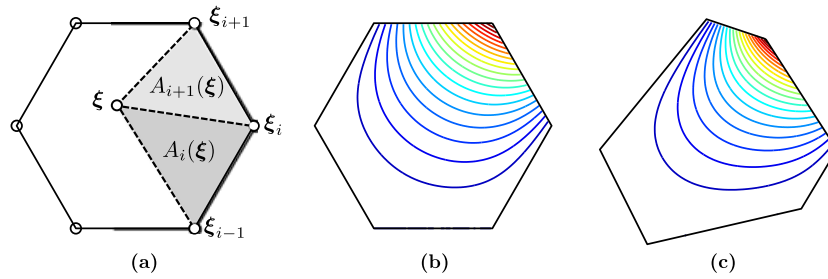


Figure 1. (a) Illustration of the triangular areas  $A_i(\xi) := A(\xi_{i-1}, \xi_i, \xi)$  used to define the interpolant  $w_i$ ; (b) contour lines of a Wachspress basis function  $\hat{\varphi}_i$  over the regular (reference) hexagon  $\hat{E}_6$ ; (c) contour lines of the ‘isoparametric’ basis function  $\varphi_i^E$  over an irregular (physical) hexagon  $E$ .

has been restricted to the interior of  $\hat{E}_n$  in order for the interpolants  $w_i$  to be well-defined, the Wachspress basis (and in fact any barycentric basis) can be extended continuously to  $\hat{E}_n$  such that if  $\xi$  lies on the edge between  $\xi_i$  and  $\xi_{i+1}$ , we have

$$\hat{\varphi}_i(\xi) = 1 - \frac{\|\xi - \xi_i\|}{\|\xi_{i+1} - \xi_i\|}, \quad \hat{\varphi}_{i+1}(\xi) = \frac{\|\xi - \xi_i\|}{\|\xi_{i+1} - \xi_i\|}, \quad \hat{\varphi}_j(\xi) = 0 \quad \forall j \neq i, i + 1 \quad (25)$$

As such, Wachspress functions are linear along the edges of the polygon and satisfy the Kronecker-delta property  $\hat{\varphi}_i(\xi_j) = \delta_{ij}$  (Figure 1(b)). Moreover, this means that properties (23) and (24) hold for all  $\xi \in \hat{E}_n$ . We remark that Wachspress functions are  $C^\infty$  in the interior of  $\hat{E}_n$ . Also, for  $n = 3$  and  $n = 4$ , that is, when  $\hat{E}_n$  is a triangle or a square, the Wachspress basis recovers the usual linear and bilinear shape functions.

We use the Wachspress basis to construct an isoparametric mapping from  $\hat{E}_n$  to any strictly convex  $n$ -gon  $E$ . If  $\mathbf{x}_1, \dots, \mathbf{x}_n$  denotes the location of the vertices of  $E$ , ordered counterclockwise, then the isoparametric map  $\mathbf{F} : \hat{E}_n \rightarrow E$  defined by

$$\mathbf{F}_E(\xi) = \sum_{i=1}^n \hat{\varphi}_i(\xi) \mathbf{x}_i \quad (26)$$

is one-to-one and onto [48]. Notice that by virtue of (25),  $\mathbf{F}_E$  maps the vertices and edges of  $\hat{E}_n$  to the corresponding vertices and edges of  $E$ . With such mapping in hand, following the standard procedure in isoparametric finite elements, we consider the following basis functions for the element  $E$

$$\varphi_i^E := \hat{\varphi}_i \circ \mathbf{F}_E^{-1}, \quad i = 1, \dots, n \quad (27)$$

and define

$$\mathcal{P}(E) = \text{span} \{ \varphi_1^E, \dots, \varphi_n^E \} \quad (28)$$

It is straightforward to show that  $\mathcal{P}(E)$  contains linear fields over  $E$  (cf. section 3.3 of [42]). Linear completeness together with their positivity implies that  $\varphi_1^E, \dots, \varphi_n^E$  are in fact barycentric coordinates for the polygon  $E$ . As a result, they are necessarily linear on the boundary  $\partial E$  and satisfy the Kronecker-delta property, that is,  $\varphi_i^E(\mathbf{x}_j) = \delta_{ij}$ .

Under appropriate shape-regularity conditions on  $E$ , the transformation map  $\mathbf{F}_E$  and its inverse remain well-behaved, and optimal interpolation estimates for  $\mathcal{V}_h$  are expected to hold. More specifically, for  $\mathbf{u} \in [H^{1+\lambda}(\Omega)]^2 \cap \mathcal{V}$ , with  $0 < \lambda \leq 1$ , we would have  $\inf_{\mathbf{v}_h \in \mathcal{V}_h} \|\mathbf{u} - \mathbf{v}_h\|_{\mathcal{V}} = \mathcal{O}(h^\lambda)$ . While such error estimates have appeared for a number of barycentric bases (along with suitable shape-regularity conditions) (cf. [49]), such analysis, to the best of our knowledge, has not been carried out for isoparametric basis functions on polygons. However, the numerical results presented

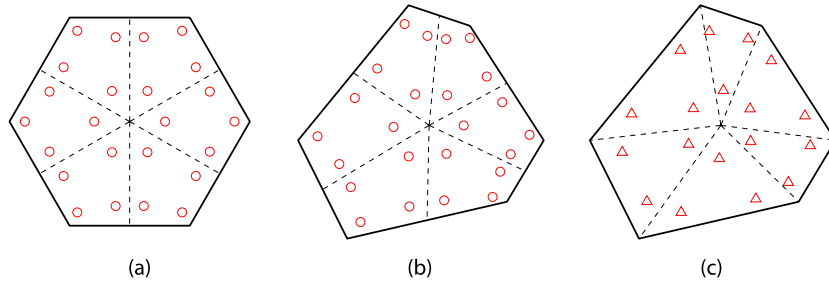


Figure 2. Illustration of the integration scheme using ‘quadrangulation’ of the polygon (a) integration points using  $2 \times 2$  Gauss quadrature for each cell of the reference hexagon; (b) location of the integration points in the physical element; (c) location of integration points in the physical element for the ‘triangulation’ scheme.

in the next section confirm this conjecture. Note that the choice of spaces  $\mathcal{V}_h$  and  $\mathcal{Q}_h$  is optimal in that both terms in the approximation errors (12)–(13) are  $\mathcal{O}(h)$  when the exact solution is sufficiently smooth.

We close this section by discussing the quadrature scheme used for evaluating the weak form integrals. For  $n = 3$  and  $n = 4$ , we use the standard quadrature rules for triangles and quads, and for  $n \geq 5$ , we divide  $\hat{E}_n$  into  $n$  quadrilaterals (by connecting the centroid to the midpoint of each edge) and use the well-known Gauss quadrature rules on each quadrilateral (cf. Figure 2). We have found that this scheme provides better accuracy compared to the triangulation approach adopted in [17, 22]. We should also note that a number of specific quadrature rules for polygonal domains have recently appeared [50, 51], although, for the purposes of this work, the adopted scheme is sufficient.

Finally, we observe that with the present choice of velocity and pressure spaces, the bilinear form  $b(\cdot, \cdot)$  can be evaluated exactly (this fact is also noted and used in [36]). Indeed, for any  $q_h \in \mathcal{Q}_h$  and  $\mathbf{v}_h \in \mathcal{V}_h$ ,

$$b(q_h, \mathbf{v}_h) = - \sum_{m=1}^M q_h|_{\Omega_m} \int_{\Omega_m} \operatorname{div} \mathbf{v}_h \, d\mathbf{x} = - \sum_{m=1}^M q_h|_{\Omega_m} \int_{\partial\Omega_m} \mathbf{v}_h \cdot \mathbf{n} \, ds \quad (29)$$

where we have used the fact that  $q_h$  is element-wise constant. Because  $\mathbf{v}_h$  varies linearly over  $\partial\Omega_m$ , the last integral can be computed using the nodal values of  $\mathbf{v}_h$ . In fact, the particular construction of barycentric basis functions over  $\Omega_m$  is immaterial for the bilinear form  $b(\cdot, \cdot)$  because all barycentric basis functions are linear on the boundary.

## 5. STABILITY AND SATISFACTION OF THE INF-SUP CONDITION

Without additional restrictions on the family of meshes  $\mathcal{T}_h$ , the pair of discrete spaces  $\mathcal{V}_h$  and  $\mathcal{Q}_h$  defined in the previous section does not necessarily satisfy the inf-sup condition. So far, we have not yet excluded the cases where  $\mathcal{T}_h$  is a triangular or quadrilateral mesh.

In [36], a set of conditions on the topology of  $\mathcal{T}_h$  that guarantees the satisfaction of the inf-sup condition for the choice of velocity and pressures defined here is identified. Although the original proof by Beirão Da Veiga and Lipnikov is given in the context of MFD, the results are applicable to the present setting because the pressure spaces are identical and  $\mathcal{V}_h$  is one particular realization of the velocity space considered in [36] when no bubble DOFs are present. Furthermore, in light of equation (29) in the previous section and equations (6) and (9) in [36], the definition of bilinear form  $b(\cdot, \cdot)$  is also identical. In fact, the main difference between the two formulations is the treatment of bilinear form  $a(\cdot, \cdot)$ .

As mentioned in the introduction, for meshes consisting of convex polygons, their result guarantees the satisfaction of inf-sup condition *if every internal node/vertex in the mesh is connected to at most three edges*. This, for example, holds for meshes obtained from a Voronoi tessellation of the domain where no four neighboring seeds lie on a circle and thus each internal vertex is incident to

exactly three edges. By contrast, a structured grid of rectangular elements violates it because the internal vertices are connected to four edges.

In practice, such convex polygonal meshes can be constructed using an appropriate Voronoi-based meshing algorithm [27, 28, 52]. While it is possible that the Voronoi tessellation of a non-convex domain from an arbitrary set of seeds contains non-convex elements near the boundary, the approach proposed in [27, 28, 52] avoids this by including additional seeds, obtained from reflections of the interior seeds about the boundary, and considering the Voronoi tessellation of the entire plane. A suitable mesh is given by a *subset* of this Voronoi diagram, which necessarily consists only of convex elements. In [28], the regularity of the mesh is ensured by requiring that the Voronoi diagram is centroidal (that is, the centroid of each element coincides with the generating seed). We will show numerical results for both random Voronoi and centroidal Voronoi (CVT) meshes in this paper.

We validate the applicability of the previous condition in the present setting by computing the stability parameter  $\beta_h$  for different families of meshes and a sequence of progressively finer meshes for each family. While this ‘test’ only furnishes a necessary condition for satisfaction of the inf-sup condition, it is shown in [53] to reliably correlate with the known theoretical results. In the following, we briefly discuss the procedure for the calculation of the stability parameter following the approach of [53].

Let us first define the space of spurious pressure modes

$$\mathcal{Q}_h^0 = \{q_h \in \mathcal{Q}_h : b(q_h, \mathbf{v}_h) = 0, \forall \mathbf{v}_h \in \mathcal{V}_h\} \quad (30)$$

and define the

$$\tilde{\beta}_h := \inf_{q_h \in (\mathcal{Q}_h^0)^\perp} \sup_{\mathbf{v}_h \in \mathcal{V}_h} \frac{b(q_h, \mathbf{v}_h)}{\|\mathbf{v}_h\|_{\mathcal{V}} \|q_h\|_{\mathcal{Q}}} \quad (31)$$

Observe that compared to  $\beta_h$  in (11), the pressure space  $\mathcal{Q}_h$  in the previous expression is replaced by the orthogonal complement of the space of pressure modes  $(\mathcal{Q}_h^0)^\perp$ . If no pressure modes exists, that is,  $\mathcal{Q}_h^0 = \{0\}$ , then  $(\mathcal{Q}_h^0)^\perp = \mathcal{Q}_h$  and so  $\tilde{\beta}_h = \beta_h$ . Otherwise, we know from previous discussion that  $\beta_h = 0$  and the discrete problem is not well-posed. The advantage of working with the restricted space is that it makes the numerical evaluation of (31) easier. Note that for a given mesh, one can directly check for the existence of pressure modes by computing the rank of the matrix associated with  $b(\cdot, \cdot)$ . However, the present procedure is also capable of detecting the presence of spurious pressure modes.

To see how  $\tilde{\beta}_h$  can be numerically evaluated, let us denote by  $\Pi_h : L_0^2(\Omega) \rightarrow \mathcal{Q}_h$  the projection operator such that for any  $g \in L_0^2(\Omega)$ ,

$$\int_{\Omega} q_h \Pi_h(g) \, d\mathbf{x} = \int_{\Omega} q_h g \, d\mathbf{x}, \quad \forall q_h \in \mathcal{Q}_h \quad (32)$$

In the case of the piecewise constant pressure space, we have the explicit expression

$$\Pi_h(g) = \sum_{m=1}^M \frac{1}{|\Omega_m|} \left( \int_{\Omega_m} g \, d\mathbf{x} \right) \chi_{\Omega_m} \quad (33)$$

With this definition, we can show that <sup>††</sup>

$$(\mathcal{Q}_h^0)^\perp = \{\Pi_h(\operatorname{div} \mathbf{w}_h) : \mathbf{w}_h \in \mathcal{V}_h\} \quad (34)$$

Therefore, we can rewrite (31) alternatively as

$$\tilde{\beta}_h = \inf_{\mathbf{w}_h \in \mathcal{V}_h} \sup_{\mathbf{v}_h \in \mathcal{V}_h} \frac{b(\Pi_h(\operatorname{div} \mathbf{w}_h), \mathbf{v}_h)}{\|\Pi_h(\operatorname{div} \mathbf{w}_h)\|_{\mathcal{Q}} \|\mathbf{v}_h\|_{\mathcal{V}}} \quad (35)$$

<sup>††</sup>Note that for any  $q_h \in \mathcal{Q}_h^0$ , we have  $\int_{\Omega} q_h \Pi_h(\operatorname{div} \mathbf{w}_h) \, d\mathbf{x} = \int_{\Omega} q_h \operatorname{div} \mathbf{w}_h \, d\mathbf{x} = 0$  for all  $\mathbf{w}_h \in \mathcal{V}_h$ .

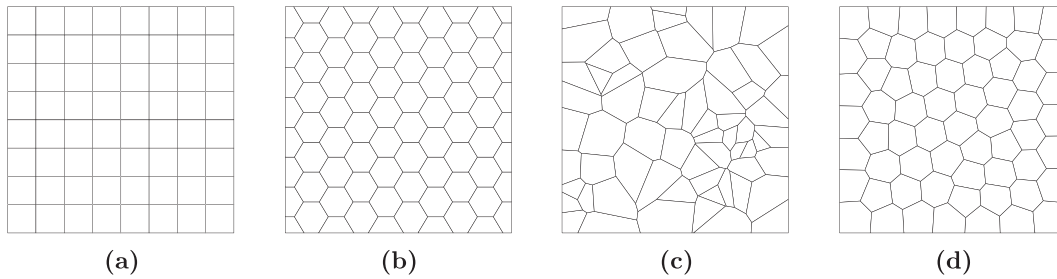


Figure 3. Representative example of the family of meshes: (a) uniform quadrilateral, (b) uniform hexagonal, (c) random Voronoi and (d) centroidal Voronoi (CVT).

Moreover, from (32), we have

$$b(\Pi_h(\operatorname{div} \mathbf{w}_h), \mathbf{v}_h) = \int_{\Omega} \Pi_h(\operatorname{div} \mathbf{w}_h) \operatorname{div} \mathbf{v}_h \, dx = \int_{\Omega} \Pi_h(\operatorname{div} \mathbf{w}_h) \Pi_h(\operatorname{div} \mathbf{v}_h) \, dx \quad (36)$$

which gives the symmetric expression

$$\tilde{\beta}_h = \inf_{\mathbf{w}_h \in \mathcal{V}_h} \sup_{\mathbf{v}_h \in \mathcal{V}_h} \frac{\int_{\Omega} \Pi_h(\operatorname{div} \mathbf{w}_h) \Pi_h(\operatorname{div} \mathbf{v}_h) \, dx}{\|\Pi_h(\operatorname{div} \mathbf{w}_h)\|_{\mathcal{Q}} \|\mathbf{v}_h\|_{\mathcal{V}}} \quad (37)$$

Let us denote by  $\{\varphi_i\}_{i=1}^{2N}$  the set of basis functions for the velocity space  $\mathcal{V}_h$  and define the following matrices associated with the terms in (37):

$$[\mathbf{S}_h]_{ij} = \int_{\Omega} \nabla \varphi_i : \nabla \varphi_j \, dx, \quad [\mathbf{G}_h]_{ij} = \int_{\Omega} \Pi_h(\operatorname{div} \varphi_i) \Pi_h(\operatorname{div} \varphi_j) \, dx \quad (38)$$

Observe that  $\mathbf{S}_h$  is positive definite and  $\mathbf{G}_h$  is positive semi-definite. We have the following relation for  $\tilde{\beta}_h$

$$\tilde{\beta}_h = \inf_{\mathbf{W} \in \mathbb{R}^{2N}} \sup_{\mathbf{V} \in \mathbb{R}^{2N}} \frac{\mathbf{W}^T \mathbf{G}_h \mathbf{V}}{(\mathbf{W}^T \mathbf{G}_h \mathbf{W})^{1/2} (\mathbf{V}^T \mathbf{S}_h \mathbf{V})^{1/2}} \quad (39)$$

From this and after some algebra, one can show that [2, 53, 54]

$$\tilde{\beta}_h = \sqrt{\lambda} \quad (40)$$

where  $\lambda$  is the smallest nonzero eigenvalue for the following eigenvalue problem

$$\mathbf{G}_h \mathbf{V} = \lambda \mathbf{S}_h \mathbf{V} \quad (41)$$

The number of spurious pressure modes can also be obtained from the eigenvalue problem (41). If there are  $k - 1$  zero eigenvalues, then there are  $\max(k - 2N + M - 1, 0)$  pressure modes present, where  $N$  and  $M$  are the total number of nodes and elements, respectively. We note that  $\tilde{\beta}_h > 0$  in such a case even though  $\beta_h = 0$  and the inf-sup condition is not satisfied.

We consider four families of meshes over the unit square  $\Omega = (0, 1)^2$ , and as in the model problem (1), the velocity boundary conditions are imposed on the entire boundary  $\partial\Omega$ . A representative mesh for each family is shown in Figure 3. For each mesh type, the quantity  $\tilde{\beta}_h$  was computed on five progressively finer meshes<sup>‡‡</sup>, and the results are shown in Figure 4. For the bilinear quads,  $\tilde{\beta}_h$  is evidently  $\mathcal{O}(h)$ , consistent with the existing theory [5] and thus decays with mesh refinement. However, this quantity remains bounded away from zero for the three types of polygonal meshes. This is the case in spite of the fact that there are few occasions in the CVT meshes where an internal edge is connected to four edges (this is due to a procedure in the algorithm proposed in [28] that collapses very small edges in the mesh into a single vertex). Finally, while a checkerboard mode is detected for every square grid, the polygonal meshes are free of any spurious pressure modes.

<sup>‡‡</sup>The mesh size is the maximum diameter of the elements in the mesh, that is,  $h = \max_m \operatorname{diam}(\Omega_m)$ .

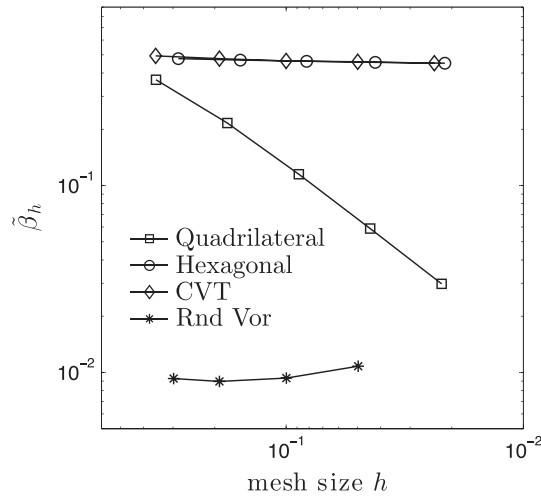


Figure 4. Computed values of the stability parameter  $\tilde{\beta}_h$  and mesh size  $h$  for different families of meshes. Note that the horizontal axis is in reverse (decreasing) order.

## 6. NUMERICAL STUDIES

In this section, we present a variety of numerical results confirming the stability and convergence of polygon finite elements and assess their performance for the families of meshes used in the previous section.

First, we consider a Stokes flow problem on the unit square  $\Omega = (0, 1)^2$  with known analytical solution given by <sup>§§</sup>

$$u_1(\mathbf{x}) = r(x_1) \sin(ax_2), \quad u_2(\mathbf{x}) = r'(x_1) \cos(ax_2)/a, \quad p(\mathbf{x}) = x_1 x_2^2 - 1/6 \quad (42)$$

where  $r(x) = (1 - x) \sin(ax)$  and  $a = 2.2\pi$ . The velocity boundary conditions on  $\partial\Omega$  as well as the body force  $\mathbf{f}$  are prescribed in accordance with (42) and  $\nu = 1$ . For polygonal elements, a second-order quadrature rule, as illustrated in Figure 2(a and b), is used. We consider 10 randomly-generated meshes for each mesh level for the random Voronoi and CVT families. In addition to the polygonal meshes, we also provide the results for uniform triangular meshes <sup>¶¶</sup> consisting of the stable MINI element [8] for the purposes of comparison.

We consider three measures for the error in the finite element solution given by

$$\|\mathbf{u} - \mathbf{u}_h\|_0, \quad \|\mathbf{u} - \mathbf{u}_h\|_\nu, \quad \|p - p_h\|_Q \quad (43)$$

The convergence plots are shown in Figure 5 where, in the case of random Voronoi and CVT meshes, the figures show the average errors and the mesh sizes for each mesh level. The results indicate that in every case, the solutions exhibit the optimal rates of convergence in the respective error norms. In fact, the  $L^2$ -error in pressure converges at a faster rate than  $\mathcal{O}(h)$  for all the mesh families. This optimal performance is even exhibited, on average, by the random Voronoi meshes despite the variations in the meshes (we note, however, that the variations of error become smaller for finer meshes). Finally, we observe that the quadrilateral discretization, while not inf-sup stable, does provide convergent velocity solutions. The pressure field, however, contains spurious checkerboard modes in every quadrilateral mesh.

As a way of comparing the performance of the different discretizations, we next plot the error as a function of number of DOFs in Figure 6. While the number of DOFs indicates the size

<sup>§§</sup>This problem is proposed and solved in [36].

<sup>¶¶</sup>The triangular meshes are obtained by splitting each element in the uniform quadrilateral grids along its left diagonal.

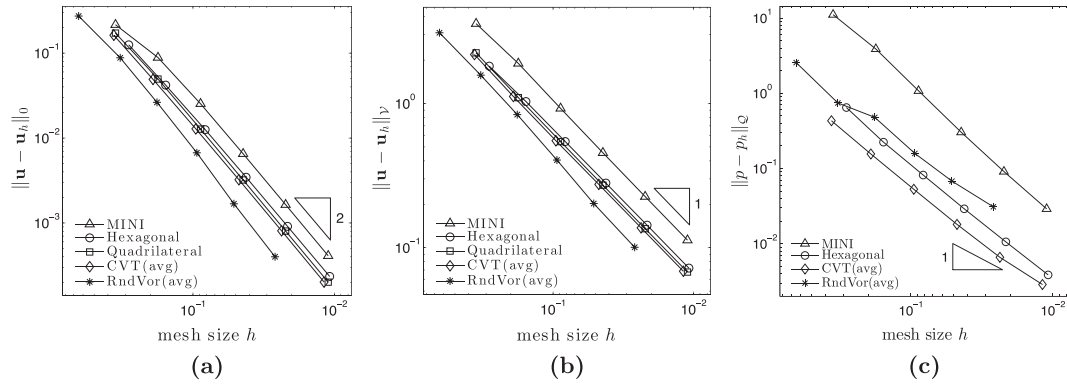


Figure 5. Plots of error versus mesh size for problem (42): (a)  $L^2$ -error in velocity, (b)  $H^1$ -error in velocity and (c)  $L^2$ -error in pressure. Note that the horizontal axis is in reverse (decreasing) order.

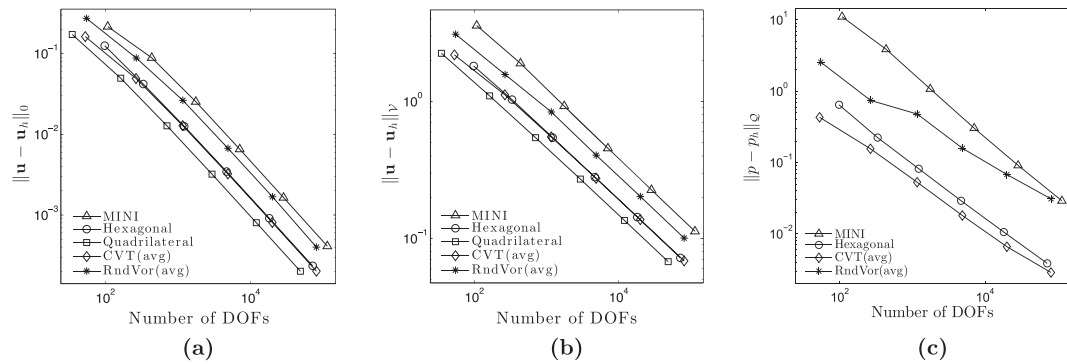


Figure 6. Plots of error versus the number of DOFs for problem (42): (a)  $L^2$ -error in velocity, (b)  $H^1$ -error in velocity and (c)  $L^2$ -error in pressure.

of the associated discrete system, it is not a perfect measure for computational performance because it does not account for the cost of computing the element matrices and the structure of the linear system and its influence of the convergence of linear solver. Nevertheless, we observe several noteworthy facts from these plots. First, the CVT and hexagonal meshes, owing to their regularity, perform better than the random Voronoi meshes. While the velocity errors are comparable for CVT and hexagonal families, CVT meshes provide more accurate pressure solutions. Also, it is interesting to note that all polygonal discretizations, including random Voronoi meshes, require a smaller number of DOFs for a given level of accuracy than the MINI discretization. The difference is pronounced for pressure solutions where, in the range of errors considered, the MINI discretization requires two orders of magnitude more DOFs than the CVT family. It is also interesting to note that the quadrilateral meshes provide better performance for the calculation for the velocity field. This may be attributed to the fact that the exact velocity field for this problem is multiplicatively separable in  $x_1$  and  $x_2$  and is thus particularly well-suited for approximation by the tensor product in quadrilateral meshes.

We also examine the error in approximating the incompressibility of the velocity field. Figure 7 shows plots of the  $L^2$ -norm of  $\text{div } \mathbf{u}_h$  as a function of mesh size and number of DOFs. We can see that the  $\text{div } \mathbf{u}_h$  converges to  $\text{div } \mathbf{u} \equiv 0$  with a linear rate in  $h$  for all mesh families. The accuracy in capturing the incompressibility constraint, in terms of the total number of DOFs, is about the same for quadrilateral, hexagonal and CVT meshes.

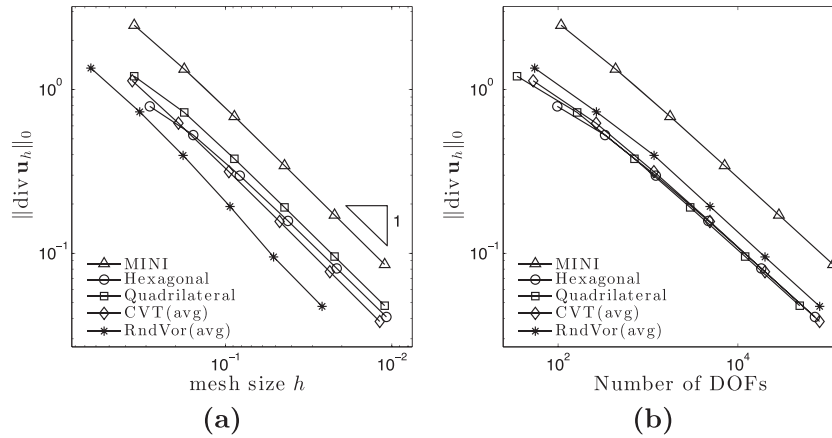


Figure 7. Plots of error in the satisfaction of the incompressibility constraint as a function of (a) mesh size  $h$  and (b) number of DOFs.

We continue our comparison of the performance of polygonal discretizations by considering the problem on the L-shaped domain  $\Omega = (-1, 1)^2 \setminus ([0, 1] \times (-1, 0])$  with exact solution given by (cf. [55])

$$\begin{aligned}
 u_1(r, \theta) &= r^\lambda [\Psi'(\theta) \cos \theta + (1 + \lambda) \sin \theta \Psi(\theta)] \\
 u_2(r, \theta) &= r^\lambda [\Psi'(\theta) \sin \theta - (1 + \lambda) \cos \theta \Psi(\theta)] \\
 p(r, \theta) &= -r^{\lambda-1} (1 - \lambda)^{-1} [(1 + \lambda)^2 \Psi'(\theta) + \Psi'''(\theta)]
 \end{aligned}
 \tag{44}$$

Here,  $(r, \theta)$  are polar coordinates with respect to the origin,

$$\begin{aligned}
 \Psi(\theta) &= (1 + \lambda)^{-1} \sin [(1 + \lambda) \theta] \cos(3\pi\lambda/2) - \cos [(1 + \lambda) \theta] \\
 &\quad - (1 - \lambda)^{-1} \sin [(1 - \lambda) \theta] \cos(3\pi\lambda/2) + \cos [(1 - \lambda) \theta]
 \end{aligned}
 \tag{45}$$

and  $\lambda$  is the smallest positive root of  $\sin(3\pi\lambda/2) - \lambda = 0$ , which is approximately  $\lambda \approx 0.54448373678246$ . The force function associated with (44) is  $\mathbf{f} = \mathbf{0}$ . Moreover, the pressure field  $p$  and velocity gradient  $\nabla \mathbf{u}$  exhibit singularity at the origin, similar to the behavior one encounters at re-entrant corners. Because  $\mathbf{u} \in [H^{1+\lambda}(\Omega)]^2$  and  $p \in H^\lambda(\Omega)$ , the optimal convergence rates of the finite element approximations for this problem are  $\mathcal{O}(h^\lambda)$  for a sequence of uniformly-refined meshes. Low-order elements are well-suited for solving this type of problems because one cannot improve convergence rates using higher-order elements.

We consider three family of meshes that are shown in Figure 8. As before, we present average results for 10 CVT meshes. Figure 9 shows plots of velocity and pressure error as a function of number of DOFs <sup>‡</sup>. As in the previous example, the computed pressure fields on the quadrilateral meshes contain spurious modes. We can see that CVT meshes, on average, provided better accuracy for both velocity and pressure approximations. The MINI discretization requires one order of magnitude more DOFs than the polygonal meshes for a given level of accuracy in the pressure field. These examples illustrate how the proposed low-order polygonal discretizations can be useful for solving problems with nonsmooth solutions.

For the next set of numerical results, we consider the classical lid-driven cavity problem for stationary Navier–Stokes flow with governing equations given by

$$(\mathbf{u} \cdot \nabla) \mathbf{u} - 2 \operatorname{div} [\nu \epsilon(\mathbf{u})] + \nabla p = \mathbf{0} \quad \text{in } \Omega
 \tag{46}$$

<sup>‡</sup>Although we have omitted the plots of error as a function of mesh size, we have observed optimal convergence rates of  $\mathcal{O}(h^\lambda)$  for all three meshes types.

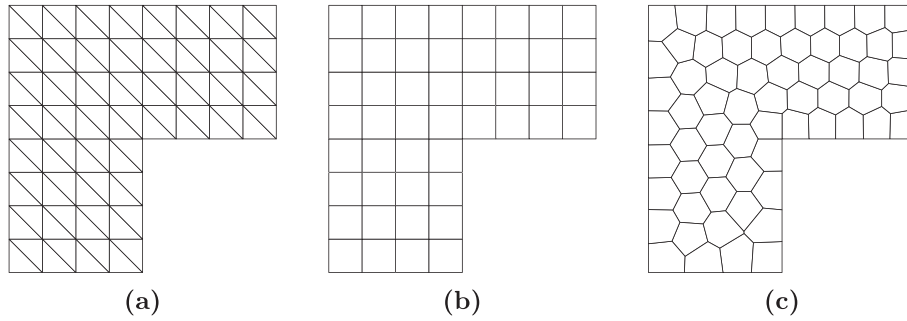


Figure 8. Representative example of the family of meshes for the L-shaped problem: (a) MINI, (b) uniform quadrilateral and (c) centroidal Voronoi.

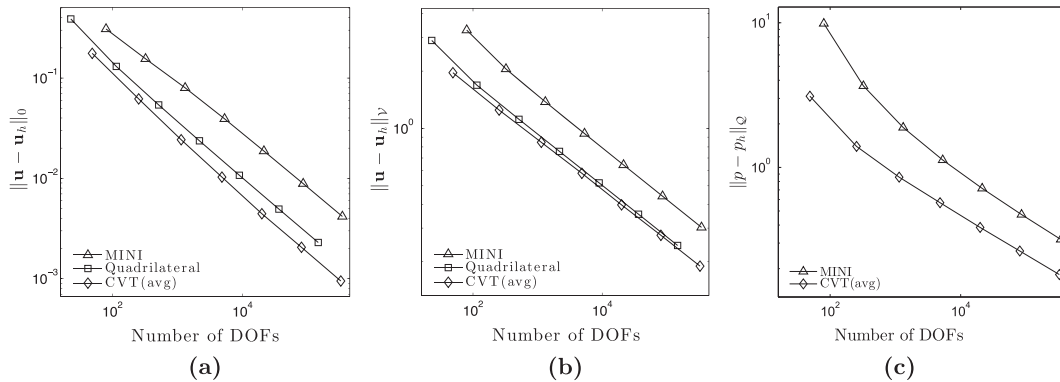


Figure 9. Plots of error versus the number of DOFs for L-shaped problem (44): (a)  $L^2$ -error in velocity, (b)  $H^1$ -error in velocity and (c)  $L^2$ -error in pressure.

subject to the incompressibility constraint. The cavity problem is posed on the unit square  $\Omega = (0, 1)^2$  with the following boundary conditions prescribed

$$\mathbf{u} = (1, 0)^T \quad \text{on } \Gamma, \quad \mathbf{u} = \mathbf{0} \quad \text{on } \partial\Omega \setminus \Gamma \tag{47}$$

Here,  $\Gamma = \{\mathbf{x} \in \partial\Omega : x_2 = 1\}$ . These correspond to stationary bottom and side walls and a horizontally moving top wall of the cavity. Because of the jump in the boundary conditions on the top two corners, there are singularities in the resulting flow at these points. In particular, the pressure and vorticity fields are not finite at the top corners. Because the characteristic velocity and length of the flow are equal to unity, the Reynolds number for this flow is given by  $\text{Re} = 1/\nu$ .

We solve the nonlinear algebraic system of equations that arise from the finite element discretization by using the classical Newton–Raphson method. For all the numerical results, we consider the ‘non-leaky’ approximation to the boundary conditions wherein no-slip conditions are imposed at the nodes located at the top two corners. We refer to [56] for an analysis of the convergence of such approximation.

First, we consider the case  $\text{Re} = 100$  and compute the extrema of horizontal and vertical velocity fields along the centerlines of the cavity as well as the vorticity  $\omega(\mathbf{u}) = \partial u_2/\partial x_1 - \partial u_1/\partial x_2$  at the center of the cavity, that is, point  $\mathbf{x} = (0.5, 0.5)^T$ . We use uniform hexagonal meshes for this study and compare the solutions to the benchmark results reported in [57]. As seen from Table I, the results indicate the convergence of finite element solutions.

Next, we plot the velocity profiles along horizontal and vertical centerlines of the cavity for  $\text{Re} = 100$  as well as the higher Reynolds number of  $\text{Re} = 1000$ . In this case, we use a fine CVT

Table I. Convergence of the extrema of the velocity through the centerlines of the cavity and the vorticity at the center of the cavity for  $Re = 100$  computed on uniform hexagonal meshes.

# Elements	$(u_1)_{\min}$	$(x_2)_{\min}$	$(u_2)_{\max}$	$(x_1)_{\max}$	$(u_2)_{\min}$	$(x_1)_{\min}$	$\omega(0.5, 0.5)$
27	-0.1935865	0.4387	0.1504861	0.2656	-0.1274992	0.6578	0.780421
80	-0.2074123	0.4767	0.1712218	0.2610	-0.2381359	0.8297	1.070017
270	-0.2119418	0.4657	0.1756644	0.2368	-0.2470137	0.7924	1.095341
986	-0.2131678	0.4650	0.1785574	0.2281	-0.2512619	0.8021	1.151346
3,729	-0.2138928	0.4599	0.1794154	0.2363	-0.2535334	0.8098	1.159909
14,560	-0.2139864	0.4588	0.1795193	0.2366	-0.2537095	0.8099	1.173501
Ref. [57]	-0.2140424	0.4581	0.1795728	0.2370	-0.2538030	0.8104	1.174412

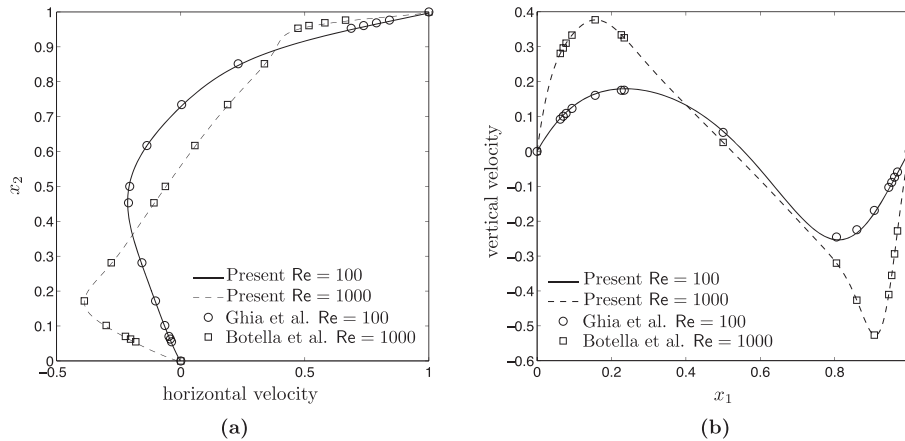


Figure 10. (a) Profile of the vertical velocity along the horizontal centerline of the cavity; (b) profile of horizontal velocity along the vertical centerline of the cavity for two different Reynolds numbers computed on a centroidal Voronoi mesh.

mesh with 65,536 elements and compare the results to those reported in [57, 58]. It is evident from Figure 10 that the computed solutions are in excellent agreement with the literature.

We remark that while the present finite element scheme can be considered as a particular case of the MFD method of [36] for Stokes flow, the same cannot be said for Navier–Stokes problems. The access to the explicit form of velocity basis functions allows for a direct extension of the method to Navier–Stokes problems, whereas to the best of the authors’ knowledge, an MFD formulation on arbitrary polygonal grids presently does not exist in this more general setting.

## 7. CONCLUDING REMARKS

In this paper, we investigated the use of polygonal finite elements for solving incompressible fluid flow problems. In particular, we examined a low-order mixed scheme on convex polygonal discretizations and established its stability and convergence. One possible extension of the present study is to consider higher-order polygonal finite elements, and the recent work of Rand *et al.* [59] on the construction of quadratic serendipity elements is relevant to such endeavor. Also of interest is the extension to three dimensions and general polyhedral-shaped finite elements. Only a handful of formulations for polyhedral discretizations are available in the literature (see, for example, [26, 60, 61]). In this regard, we also note the work of Beirão Da Veiga *et al.* [62] on a low-order MFD formulation of Stokes flow on polyhedral meshes, which is shown to be stable when edge bubble DOFs are included in the velocity approximation. We anticipate that under certain topological conditions imposed on the mesh, perhaps similar to those discussed here, these additional DOFs may not be needed for stability.

## ACKNOWLEDGEMENTS

The authors appreciate constructive comments and insightful suggestions from the anonymous reviewers. Ivan F. M. Menezes and Anderson Pereira acknowledge the financial support provided by Tecgraf/PUC-Rio (Group of Technology in Computer Graphics), Rio de Janeiro, Brazil. We are thankful to the support from the US National Science Foundation under grant CMMI #1321661 and from the Donald B. and Elizabeth M. Willett endowment at the University of Illinois at Urbana-Champaign. Any opinion, finding, conclusions or recommendations expressed here are those of the authors and do not necessarily reflect the views of the sponsors.

## REFERENCES

1. Girault V, Raviart PA. *Finite Element Method for Navier-Stokes Equations*. Springer Verlag: Berlin, 1986.
2. Brezzi F, Fortin M. *Mixed and Hybrid Finite Element Method*. Springer: New York, 1991.
3. Donea J, Huerta A. *Finite Element Methods for Flow Problems*. John Wiley and Sons, Ltd.: West Sussex, England, 2003.
4. Ern A, Guermond JL. *Theory and Practice of Finite Elements*. Springer Verlag: New York, 2004.
5. Boffi D, Brezzi F, Fortin M. Finite elements for the Stokes problem. *Lecture Notes in Mathematics* 2008; **1939**:45–100.
6. Babuska I. Error bounds for finite element method. *Numerical Mathematics* 1971; **18**:322–333.
7. Brezzi F. On the existence, uniqueness and approximation of saddle-point problems arising from lagrangian multipliers. *RAIRO Analyse Numérique* 1974; **8**(R.2):129–151.
8. Arnold DN, Brezzi F, Fortin M. A stable finite element for the Stokes equations. *Calcolo* 1984; **21**(4): 337–344.
9. Hughes TJ, Franca LP, Balestra M. A new finite element formulation for computational fluid dynamics: V. Circumventing the Babuska-Brezzi condition: a stable Petrov-Galerkin formulation of the Stokes problem accommodating equal-order interpolations. *Computer Methods in Applied Mechanics and Engineering* 1986; **59**(1): 85–99.
10. Brezzi F, Douglas JJ. Stabilized mixed methods for the Stokes problem. *Numerical Mathematics* 1988; **53**: 225–236.
11. Barth T, Bochev P, Gunzburger M, Shadid J. A taxonomy of consistently stabilized finite element methods for the Stokes problem. *SIAM Journal on Scientific Computing* 2004; **25**(5):1585–1607.
12. Silvester D. Optimal low order finite element methods for incompressible flow. *Computer Methods in Applied Mechanics and Engineering* 1994; **111**:357–368.
13. Bochev PB, Dohrmann CR, Gunzburger MD. Stabilization of low-order mixed finite elements for the Stokes equations. *SIAM Journal on Numerical Analysis* 2006; **44**(1):82–101.
14. Tallec PL, Ruas V. On the convergence of the bilinear-velocity constant-pressure finite element method in viscous flow. *Computer Methods in Applied Mechanics and Engineering* 1986; **54**(2):235–243.
15. Hauret P, Kuhl E, Ortiz M. Diamond elements: a finite element/discrete-mechanics approximation scheme with guaranteed optimal convergence in incompressible elasticity. *International Journal for Numerical Methods in Engineering* 2007; **72**:253–294.
16. Talischi C, Paulino GH, Le CH. Honeycomb Wachspress finite elements for structural topology optimization. *Structural and Multidisciplinary Optimization* 2009; **37**(6):569–583.
17. Talischi C, Paulino GH, Pereira A, Menezes IFM. Polygonal finite elements for topology optimization: a unifying paradigm. *International Journal for Numerical Methods in Engineering* 2010; **82**(6):671–698.
18. Saxena A. A material-mask overlay strategy for continuum topology optimization of compliant mechanisms using honeycomb discretization. *Journal of Mechanical Design* 2008; **130**(8):082304.
19. Langelaar M. The use of convex uniform honeycomb tessellations in structural topology optimization. *Proceedings of 7th World Congress on Structural and Multidisciplinary Optimization*, 2007; 21–25.
20. Jog CS, Haber RB. Stability of finite element models for distributed-parameter optimization and topology design. *Computer Methods in Applied Mechanics and Engineering* 1996; **130**(3-4):203–226.
21. Wachspress EL. *A Rational Finite Element Basis*. Academic Press: New York, 1975.
22. Sukumar N, Tabarraei A. Conforming polygonal finite elements. *International Journal for Numerical Methods in Engineering* 2004; **61**(12):2045–2066.
23. Sukumar N, Malsch EA. Recent advances in the construction of polygonal finite element interpolants. *Archives of Computational Methods in Engineering* 2006; **13**(1):129–163.
24. Ghosh S. *Micromechanical Analysis and Multi-scale Modeling Using the Voronoi Cell Finite Element Method*. CRC Press: Florida, 2011.
25. Talischi C, Paulino GH, Pereira A, Menezes IFM. PolyTop: A Matlab implementation of a general topology optimization framework using unstructured polygonal finite element meshes. *Structural and Multidisciplinary Optimization* 2012; **45**:329–357.
26. Rashid MM, Selimotic M. A three-dimensional finite element method with arbitrary polyhedral elements. *International Journal for Numerical Methods in Engineering* 2006; **67**(2):226–252.

27. Bolander JE, Saito S. Fracture analyses using spring networks with random geometry. *Engineering Fracture Mechanics* 1998; **61**(5-6):569–591.
28. Talischi C, Paulino GH, Pereira A, Menezes IFM. PolyMesher: a general-purpose mesh generator for polygonal elements written in Matlab. *Structural and Multidisciplinary Optimization* 2012; **45**:309–328.
29. Sieger D, Alliez P, Botsch M. Optimizing Voronoi diagrams for polygonal finite element computations. *Proceedings of the 19th International Meshing Roundtable*, 2010; 435–350.
30. Ebeida MS, Mitchell SA. Uniform random Voronoi meshes. *Proceedings of the 20th International Meshing Roundtable*, 2012; 273–290.
31. Brezzi F, Lipnikov K, Shashkov M, Simoncini V. A new discretization methodology for diffusion problems on generalized polyhedral meshes. *Computer Methods in Applied Mechanics and Engineering* 2007; **196**(37-40): 3682–3692.
32. Brezzi F, Buffa A, Lipnikov K. Mimetic finite differences for elliptic problems. *ESAIM Mathematical Modelling and Numerical Analysis* 2009; **43**(02):277–295.
33. Beirão Da Veiga L, Lipnikov K, Manzini G. Arbitrary-order nodal mimetic discretizations of elliptic problems on polygonal meshes. *SIAM Journal on Numerical Analysis* 2011; **49**(5):1737–1760.
34. Beirão Da Veiga L, Brezzi F, Cangiani A, Manzini G, Marini LD, Russo A. Basic principles of Virtual Element Methods. *Mathematical Models and Methods in Applied Sciences* 2013; **23**:199–214.
35. Beirão Da Veiga L, Gyrya V, Lipnikov K, Manzini G. Mimetic finite difference method for the Stokes problem on polygonal meshes. *Journal of Computational Physics* 2009; **228**(19):7215–7232.
36. Beirão Da Veiga L, Lipnikov K. A mimetic discretization of the Stokes problem with selected edge bubbles. *SIAM Journal on Scientific Computing* 2010; **32**(2):875–893.
37. Pierre R. Simple  $C^0$  approximations for the computation of incompressible flows. *Computer Methods in Applied Mechanics and Engineering* 1988; **68**(2):205–227.
38. Brenner SC, Scott LR. *The Mathematical Theory of Finite Element Methods*, 2nd ed. Springer: New York, 2002.
39. Malkus DS, Olsen ET. Obtaining error estimates for optimally constrained incompressible finite elements. *Computer Methods in Applied Mechanics and Engineering* 1984; **45**:331–353.
40. Boland J, Nicolaides R. On the stability of bilinear-constant velocity-pressure finite elements. *Numerical Mathematics* 1984; **44**(2):219–222.
41. Boland J, Nicolaides R. Stable and semistable low order finite elements for viscous flows. *SIAM Journal on Numerical Analysis* 1985:474–492.
42. Hughes TJR. *The Finite Element Method: Linear Static and Dynamic Finite Element Analysis*. Dover Publications: New York, 2000.
43. Sani RL, Gresho PM, Lee RL, Griffiths DF. The cause and cure (?) of the spurious pressures generated by certain FEM solutions of the incompressible Navier-Stokes equations: Part 1. *International Journal for Numerical Methods in Fluids* 1981; **1**(1):17–43.
44. Sani RL, Gresho PM, Lee RL, Griffiths DF, Engelman M. The cause and cure (!) of the spurious pressures generated by certain FEM solutions of the incompressible Navier-Stokes equations: Part 2. *International Journal for Numerical Methods in Fluids* 1981; **1**(2):171–204.
45. Bochev P, Lehoucq RB. On finite element solution of the pure Neumann problem. *SIAM Review* 2001; **47**:50–66.
46. Floater MS, Hormann K, Kos G. A general construction of barycentric coordinates over convex polygons. *Advances in Computational Mathematics* 2006; **24**(1-4):311–331.
47. Meyer M, Barr A, Lee H, Desbrun M. Generalized barycentric coordinates on irregular polygons. *Journal of Graphics Tools* 2002; **7**:13–22.
48. Floater MS, Kosinka J. On the injectivity of Wachspress and mean value mappings between convex polygons. *Advances in Computational Mathematics* 2010; **32**(2):163–174.
49. Gillette A, Rand A, Bajaj C. Error estimates for generalized barycentric interpolation. *Advances in Computational Mathematics* 2012; **37**(3):417–439.
50. Mousavi SE, Xiao H, Sukumar N. Generalized Gaussian quadrature rules on arbitrary polygons. *International Journal for Numerical Methods in Engineering* 2010; **82**(1):99–113.
51. Natarajan S, Bordas S, Mahapatra DR. Numerical integration over arbitrary polygonal domains based on Schwarz-Christoffel conformal mapping. *International Journal for Numerical Methods in Engineering* 2009; **80**(1):103–134.
52. Yip M, Mohle J, Bolander JE. Automated modeling of three-dimensional structural components using irregular lattices. *Computer-Aided Civil and Infrastructure* 2005; **20**(6):393–407.
53. Chapelle D, Bathe KJ. The inf-sup test. *Computers and Structures* 1993; **47**(4-5):537–545.
54. Malkus DS. Eigenproblems associated with the discrete LBB condition for incompressible finite elements. *International Journal of Engineering Science* 1981; **19**(10):1299–1310.
55. Gerdes K, Schotzau D. hp-finite element simulations for Stokes flow – stable and stabilized. *Finite Elements in Analysis and Design* 1999; **33**:143–165.
56. Cai Z, Wang Y. An error estimate for two-dimensional Stokes driven cavity flow. *Mathematical and Computer* 2009; **78**(266):771–787.
57. Botella O, Peyret R. Benchmark spectral results on the lid-driven cavity flow. *Computers and Fluids* 1998; **27**(4):421–433.
58. Ghia U, Ghia KN, Shin T. High-Re solutions for incompressible flow using the Navier-Stokes equations and a multigrid method. *Journal of Computational Physics* 1982; **48**(387-411).

59. Rand A, Gillette A, Bajaj C. Quadratic serendipity finite element on polygons using generalized barycentric coordinates, 2012. *arXiv:1109.3259v2 [math.NA]*.
60. Hormann K, Sukumar N. Maximum entropy coordinates for arbitrary polytopes. *Eurographics Symposium on Geometry Processing* 2008; **27**(5).
61. Milbradt P, Pick T. Polytope finite elements. *International Journal for Numerical Methods in Engineering* 2008; **73**(12):1811–1835.
62. Beirão Da Veiga L, Lipnikov K, Manzini G. Error analysis for a mimetic discretization of the steady stokes problem on polyhedral meshes. *SIAM Journal on Numerical Analysis* 2010; **48**(4):1419–1443.